Fatigue performances of FSW and GMAW aluminum alloys welded joints: Competition between microstructural and structural-contact-fretting crack initiation

Damien Texier, F. Atmani, P. Bocher, F. Nadeau, Jie Chen, Y. Zedan, N. Vanderesse, V. Demers

Fatigue performances of FSW and GMAW aluminum alloys welded joints: Competition between microstructural and structural-contact-fretting crack initiation

D. Texier[1,2,*], F. Atmani[1], P. Bocher[1], F. Nadeau[3], J. Chen[1], Y. Zedan[1], N. Vanderesse[1], V. Demers[1]

[1] École de technologie supérieure, Department of Mechanical Engineering, 1100 Notre-Dame West, Montreal, H3C 1K3, QC, Canada

[2] Institut Clément Ader (ICA), Université de Toulouse, CNRS, INSA, UPS, Mines Albi, ISAE-SUPAERO, Campus Jarlard, 81013 Albi Cedex 09, France

[3] National Research Council Canada, Aluminium Technology Centre, 501 University Boulevard East, Saguenay, G7H 8C3, QC, Canada

* **Corresponding author:** Damien TEXIER. Phone: +33.(0)5.63.49.31.05

Abstract:

The fatigue properties of gas metal arc welded and friction stir welded assemblies made of aluminum alloy AA6061-T6 structural extrusions were examined. The mechanical performances of welded joints were obtained using uniaxial tensile and force-controlled constant amplitude axial fatigue tests. Microstructural and fractographic analyses were conducted to document the influence of the process on microstructure evolution, fatigue crack initiation sites, and propagation mechanisms leading to the final rupture of the assemblies. Microhardness measurements and digital image correlation techniques paired with interrupted tensile tests were also used to investigate the complex heterogeneous local mechanical behavior and to highlight the fact that the crack initiation mechanism was driven by the microstructural state of the joint as well as by the structural-contact-fretting occurring at the notch root. The corresponding fatigue strengths at 2 million and 10 million cycles were evaluated respectively at 10% and 20% higher for friction stir welded assemblies versus gas metal arc welded assemblies. Fractographic analyses revealed that the fatigue cracks were initiated from microstructural features (pores for the GMAW configuration and banded structure

on the crown side for the FSW configuration), or from large sub-surface grains in a shallow region below the structural-contact-fretting occurring at the notch root.

Keywords: Aluminum alloys; FSW; GMAW; Fatigue; Digital image correlation (DIC).

I. Introduction

High strength precipitation hardened aluminum alloys (AA) exhibit relatively high mechanical performances combined with low densities, leading to high specific strength properties suitable in many industrial sectors. Specifically, these high performance materials are increasingly used in the transportation industry for their high weight and cost reduction potential for large structural components and assemblies[1,2]. AA6XXX series aluminum alloys, including AA6061-T6 alloy, also demonstrate remarkable weldability using conventional and advanced methods, as well as an appreciable formability for complex extrusion profiles, making them good material candidates for large and complex shape welded structural components[3,4]. However, transportation manufacturers are facing several technological challenges in overcoming the structural durability of welded assemblies subjected to cyclic stresses[5]. Among the variety of potential liquid- and solid-state joining techniques available for mass production, the gas metal arc welding (GMAW) and the friction stir welding (FSW) processes are widely used in the land transport industry. Each of these techniques has specific advantages and limitations arising from the physical properties of aluminum alloys, such as high solidification shrinkage, high coefficient of thermal expansion, high thermal conductivity, relatively large solidification temperature range, sensitivity to oxide formation, and high solubility of hydrogen in liquid state[6].

The GMAW process is a conventional liquid-state welding process for mass production allowing high welding speed, deep penetration, and high deposition rate; resulting in an attractive process for assembling large components. In return, the high heat input generally required for the formation of the fusion pool (*i.e.*, melting of the base material (BM) and the filler material) affects the mechanical properties of the assemblies: defects are found within the weld passes (porosity, lack of fusion, hot cracking), unavoidable and heterogeneous residual stress distributions are present over the welded joint region, and the base material is significantly softer within the heat-affected zone (HAZ) generated during the welding operation, subsequently impairing the in-service performance of the assemblies. Malin[7] reported that an area of minimum hardness (53 to 66% of the base material hardness) within the HAZ for AA6061-T6 GMAW assemblies - located in 0.5 to 13.0 mm range from the fusion line, depending on the welding variables - was intimately linked to a reversion of strengthening precipitates (as the local maximal temperature is close to the solvus temperature of rod-shaped β’

precipitates and significantly higher than the solvus temperature of needle-shaped β''-precipitates). This area of minimum hardness within the HAZ also corresponds to the location of tensile failure, irrespective of the heat input during the welding operation. This leads to a considerable loss of mechanical performance as compared to the initial base material (Tensile strength$_{joint}$/Tensile strength$_{BM}$ ≈ 58 to 71%). In addition, several research teams have highlighted the fact that higher mechanical performance is generally associated with narrower regions of minimum hardness found closer to the fusion line[8–12]. Stathers *et al.*[12] experimentally demonstrated that the microhardness was a robust characterization tool for predicting the tensile properties within the HAZ, *i.e.* both the yield strength (YS) and the ultimate tensile strength (UTS). As far as cyclic stresses are concerned, welding defects inherent to the GMAW process are prone to crack initiation, which significantly reduces the fatigue performance of welded assemblies as compared to the base material[9,13]. Specifically, da Silva *et al.*[14] reported that fatigue cracks initiate at the weld toe (*i.e.*, at the interface of the welding pass and the HAZ) due to the combined effects of higher porosity, lack of wetting, and change of geometry due to the filler material reinforcement, resulting in high stress concentration in the toe weld region[9,14].

The FSW process is a solid-state welding technique, in which the assembly is locally heated and mixed using a mechanical pressure applied by a rotating tool on the material[15]. This welding method was developed 25 years ago to join materials traditionally considered "unweldable" with conventional fusion processes[16]. The FSW process is characterized by a significant reduction in heat input, resulting in the limitation of volumetric defects typically found in the liquid-state welding technique. However, the thermal cycle experienced during the FSW process is sufficient to form a HAZ in AA6061-T6, and the hardness of the HAZ (HV_{HAZ}^{FSW} = 65 ± 10 HV) is comparable to or slightly higher than that for the GMAWed configurations[17–21]. Dissymmetry in hardness profiles was reported for AA6XXX-T6 FSWed assemblies, with the HAZ on the retreating side being slightly softer[17,19,21]. The mechanical performances of AA6061-T6 FSWed assemblies and the fracture location under monotonic tensile tests were found to be highly sensitive to the revolutionary pitch and advancing speed of the tool – thus to the heat input – as reported by Liu *et al.*[17], with optimum properties (YS_{joint}/YS_{BM} ≈ 58% and UTS_{joint}/UTS_{BM} ≈ 77%) found at a revolutionary pitch of 0.53 mm·rev^{-1}. Fuji *et al.*[18] had similar statements about the outcome of the revolutionary pitch, but also a

slight influence of the tool geometry on the weld mechanical performances. By testing tensile specimens from different typical regions of FSWed assemblies (*i.e.* the nugget zone (NZ), the thermomechanical affected zone (TMAZ) and the heat-affected zone (HAZ)), Woo *et al.*[20] reported that the HAZ demonstrated a higher yield strength (YS_{HAZ}^{FSW} = 242 MPa while YS_{TMAZ}^{FSW} = 150 MPa and YS_{NZ}^{FSW} = 160 MPa) as compared to the TMAZ and NZ regions, but a lower ultimate tensile strength (UTS_{HAZ}^{FSW} = 290 MPa while UTS_{TMAZ}^{FSW} = 315 MPa and UTS_{NZ}^{FSW} = 380 MPa)[20]. Under cyclic loading, cracks were reported to propagate within the stirred region, with the crack initiation location evolving as the revolutionary pitch and the applied stress amplitude were increased, *i.e.* from the limit of the tool shoulder on the crown side to the center of the weld[9,21]. Das *et al.* highlighted that a variation of the revolutionary pitch from 0.13 to 0.08 mm·rev^{-1} leads to a drop of one order of magnitude in fatigue life[21]. Recent studies have shown that local plastic strain localization develops near the limit of the tool shoulder under monotonic tensile[22] and cyclic stresses[23]; these strain localization regions being strongly prone to fatigue crack initiation. In addition, FSWed assemblies generally demonstrated higher fatigue properties than other conventional or advanced liquid-state joined assemblies despite comparable yield strength and ultimate tensile strength properties[9,13]. As a comparison, Moreira *et al.* reported that AA6061-T6 FSWed assemblies exhibit a fatigue lifespan that is three times higher, at stresses close to the yield strength and a fatigue limit at least 35 to 40 MPa higher than that of GMAWed assemblies[9].

Most of the studies reported in the literature are performed on butt configurations. However, the design of large welded components occasionally requires more intricate welding configurations than the conventional butt configuration, and a permanent backing plate configuration is usually required for positioning purposes. The permanent backing plate aims at helping the alignment of large structural components during the welding operation[24,25].The fatigue properties of such structures have received very little attention in the literature even though they are extensively used in the industry. Therefore, the objective of this work is to characterize the high-cycle fatigue performances of GMAW and FSW processed structural assemblies made of extruded AA6061-T6, using butt welds with permanent backing plate configurations, and to investigate their fatigue behavior using fractographic analysis, metallographic analysis, x-ray microtomography, microhardness, and the digital image correlation (DIC) technique. This latter technique aimed at quantitatively evaluating softened regions on the welded

assemblies subjected to crack initiation, as demonstrated in butt-FSWed joints with multiple microstrain-gages[23].

II. Material and experimental methods

II.1. Material

The base material (BM) used in the present study was an extruded profile AA6061-T6 aluminum alloy having a thickness of 9.4 mm. This structure was specifically designed for butt-welding operation on structural components with an overlap for positioning the assembly during the welding operation (Fig. 1.a and b). The blue (BM #1) and red (BM #2) components in Fig. 1.a and b represent the original design of the two extruded profiles prior to welding using a permanent backing plate (also shown in Fig. 1.c and d). The T6 condition corresponds to a solution heat treatment followed by an artificial aging treatment. Joint assemblies were carried out using the gas metal arc welding (GMAW) and friction stir welding (FSW) processes. The chemical composition of the base material (AA6061) and of the filler material (AWS ER5356, Ø 1.2 mm) used during the GMAW operation are reported in Table 1.

Table 1: Chemical composition of the base material (AA6061-T6) for the two welding processes and of the filler material (AWS ER5356) for the GMAW process (wt. %)

	Si	Fe	Cu	Mn	Mg	Cr	Zn	Ti	Al
AA6061	0.40 - 0.80	0.70	0.15 - 0.40	0.15	0.80 - 1.20	0.04- 0.35	0.25	0.15	Bal.
AWS ER5356	0.25	0.40	0.10	0.05 - 0.20	4.5 – 5.5	0.05 – 0.20	0.1	0.06 - 0.20	Bal.

II.2. Welding processes

The GMAW configuration consisting of a half V-groove butt was welded using three passes, as depicted in Fig. 1.a. The arc voltage, the welding current, and the travel speed were 23 V, 240 A, and 500 mm·min^{-1}for the first pass, 24.7 V, 237 A, and 450 mm·min^{-1} for the second pass, and 24.9 V, 236 A, and 450 mm·min^{-1} for the third pass, respectively. The three welding passes were performed using the same wire feed speed (14 m·min^{-1}) under high purity argon inert gas. These welding parameters were chosen based on a preliminary investigation, tensile and microstructural characterizations. The goal was to limit the heat input while having

a full penetration of the weld and a uniform microstructure, minimizing defects/pores in the fusion zone. The welding direction (WD) for all investigated welding configurations was aligned with the extrusion direction (ED) of the base material. For more clarity, a reference system showing the welding direction (WD), the cross-welding direction (CWD), and the normal direction (ND) is included with most of the figures presented below. A typical cross-section macrograph of the assembly obtained by the GMAW process is illustrated in Fig. 1.c, showing the occurrence and the size of pores within the three weld passes. Note that millimeter-scale pores were seen, particularly within the first and second passes, and a lighter gray level in a neighboring area of the three passes was also visible, showing the extension of the heat-affected zone (HAZ) in the base material due to the welding operation (confirmed with microhardness profiles presented in section III.4).

The same two extruded profiles were butt-welded using the FSW operation (Fig. 1.b). The welding parameters were as follows: forge force control set at 17 kN, rotating speed of 1200 $rev \cdot min^{-1}$, and advancing speed of 400 $mm \cdot min^{-1}$ (0.33 $mm \cdot rev^{-1}$). The shoulder diameter of the FSW tool was 21.5 mm, the pin diameter was 8.5 mm at the shoulder zone and 6.5 mm at the pin end zone, while the pin length was 10.5 mm. As for the GMAW process, a preliminary investigation aimed at selecting the present optimum welding parameters for the FSW process. These FSW parameters were dedicated to further robotic use in industrial industry, thus limiting the admissible load during the welding process (slightly hot joint parameters, minimal shoulder diameter), limiting the occurrence of welding defects (kissing bond and tunneling) and limit longitudinal stresses in order to protect the tool with relatively high rotation speed and low advance speed. The macrostructure of the joint (Fig. 1.d) shows the nugget zone (NZ), the thermo-mechanically affected zone (TMAZ), and the heat-affected zone (HAZ). The mixing of the two structural components within the NZ is clearly visible in the central area of Fig. 1.d (also schematically represented in Fig. 1.b).

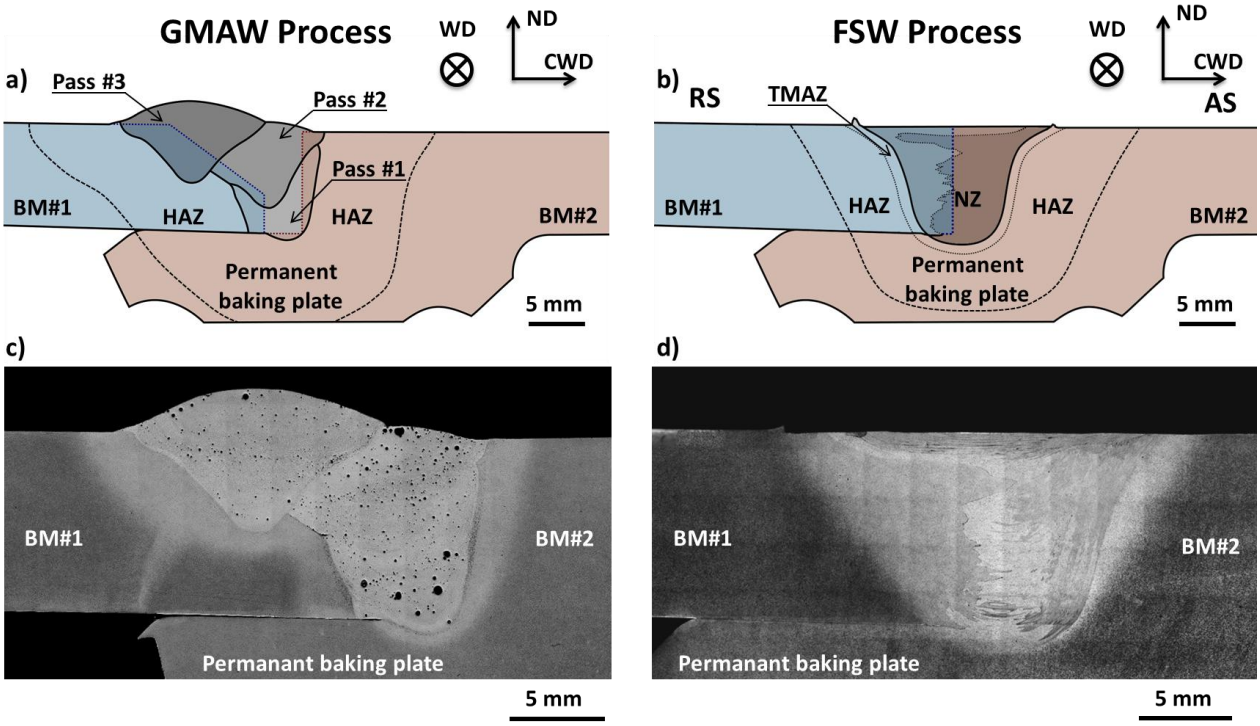

Fig. 1: Cross-section view of the GMAW process and FSW process configurations: Schematic illustrations of the design of the structural components a) prior to GMAWelding, where the three welding passes were superimposed and the heat-affected zone (HAZ) was shown and, b) prior to FSWelding, where a mixing area after welding was superimposed and the nugget zone (NZ), the thermo-mechanically affected zone (TMAZ) and the heat-affected zone (HAZ) were shown, and c) macrograph showing the different passes of the weld and the HAZ in a neighboring area of the weld. Micrometer- and millimeter-size pores (black dots) were found within the three passes of the weld. Millimeter-size pores were particularly found within passes #1 and #2; d) macrograph showing the delimitation of the interface of NZ/TMAZ and the mixing of the two original structural components within the NZ.

II.3. Specimen preparation for the mechanical testing

Tensile and fatigue specimens were machined from the welded assemblies according to the specimen geometry proposed in the ASTM-E466 standard (Fig. 2). The present specimen geometry is a model geometry representative of a train wall for railway application. Such a design is allowed in the DVS 1608: “Design and strength assessment of welded structures from aluminium alloys in railway applications” and by the International Institute of Welding (IIW):

"Recommendations for Fatigue Design of Welded Joints and Components". The weld was transverse to the loading direction for all joint configurations, and centered in the gage length of the specimen. The sharp edges of fatigue specimens were broken, while the edge of the specimen previously machined (*i.e.* perpendicular to WD in Fig. 2) were mirror-polished using successively finer grits of abrasive SiC papers, and then cloths with 1 µm diamond particles to minimize the effect of surface finish and produce uniform reproducible surfaces. No surface preparation was carried out for the top and bottom sides of the assemblies (*i.e.* perpendicular to the normal direction (ND) in Fig. 2). For the macroscopic stress calculation, the gage-section of the specimen was considered as the minimal initial gage section prior to welding, *i.e.* approximatively 9.4×19 mm^2 as shown in Fig. 2. The thickness and width are measured for all the specimens prior to fatigue testing due to geometrical tolerances after machining and surface preparation.

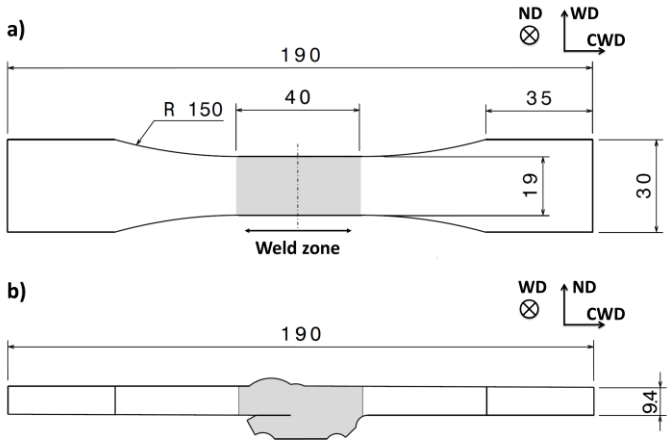

Fig. 2: Geometry of the tensile and fatigue specimens according to ASTM-E466 standard (dimensions in millimeters). The weld was centered in the specimen gage for the two weld configurations: a) top view, b) side view, for the GMAW configuration.

II.4. Tensile testing

Tensile tests were conducted at room temperature using a MTS Landmark (100 kN) servo-hydraulic testing machine according to ASTM E8 standard. AA6061-T6 base material, GMAW, and FSW configurations were tested up to fracture (Table 2) to assess macroscopic tensile properties such as the 0.2% offset yield stress (YS) and the ultimate tensile strength (UTS) which were used to define the limits of the high-

cycle-fatigue testing domain. Tensile tests performed with the base material samples were conducted along the transverse direction of the extruded base material, *i.e.* in the same direction as the GMAW and the FSW specimens. As expected, the weld configurations exhibited lower static mechanical strengths than did the base material (Table 2). Although both welded configurations exhibited similar ultimate tensile strengths, the FSW configuration demonstrated slightly higher macroscopic yield strength than the GMAW configuration (≈ 10%).

Table 2: Mechanical proprieties of the AA6061-T6 base material and welded assemblies obtained by the GMAW and the FSW processes.

	YS (MPa)	**UTS (MPa)**	**YS_{joint}/ YS_{BM}**	**UTS_{joint}/ UTS_{BM}**
Extruded AA6061-T6 base material (BM)	244.5 ± 0.3	281.3 ± 0.7	-	-
GMAW configuration	138.1 ± 0.7	231.9 ± 0.2	0.57	0.82
FSW configuration	154.4 ± 1.4	231.2 ± 1.1	0.63	0.82

II.5. Fatigue testing

Uniaxial high-cycle fatigue (HCF) tests were performed at room temperature using a MTS Landmark (100 kN) servo-hydraulic machine according to ASTM E466 standard. HCF tests were conducted under load control, using sinusoidal loading amplitudes, a positive load ratio $R_\sigma = 0.67$ (typical load ratio experienced by train walls for railway application), and a frequency of 20 Hz, up to fracture or 10^7 cycles, which was set as the run-out condition. Five different stress amplitude levels (*i.e.* $\sigma_a = 0.5[\sigma_{max} - \sigma_{min}]$) ranging from 18 to 35 MPa were chosen to obtain the S-N curves in the range of 10^5 to 10^7 cycles. The maximum applied stress (σ_{max}) associated with the maximum stress amplitude level was equivalent to 75% of the UTS of each welded assembly. For both welded configurations, each stress level was repeated at least three times with different specimens.

II.6. Metallographic characterizations

Specimens for metallographic characterizations were extracted from the weld assemblies with a precision cutting machine, cold-mounted in epoxy resin, and then mirror-polished using a 1 µm diamond paste. Specimens were finally chemically etched with a Keller solution (2 mL HF (48% vol.), 3 mL HCl (35% vol.), 5 mL HNO_3 (60% vol.) diluted in 190 mL H_2O) to reveal the microstructure in the ND/CWD cross-section plane.

II.7. Microhardness measurements

Vickers microhardness measurements were performed using an automated CLEMEX apparatus (load of 50 gf applied during a dwell time of 10 s). Specimens for microhardness measurements were mounted in the CWD-ND plane (*e.g.,* as represented in Fig. 1) and polished using the metallographic procedure detailed above. Three microhardness profiles along the cross-welding direction were carried out along the normal direction (ND). These profiles aimed to quantify the change in local properties of the joints as well as identify the typical regions such as the HAZ, the TMAZ, and the FZ or NZ encountered within GMAW and FSW welded assemblies.

II.8. Tomographic analyses

Welding configurations were examined by X-ray microtomography using a XT H 225 scanner (Nikon Metrology Inc.). Projections were obtained with a tube potential of 140 kV, and a tube current of 210 µA using a 0.5 mm thickness copper filter. In all, 2634 projections were done to cover the 360° rotation of each sample. The numerical resolution for the 3D volume reconstruction with these parameters was 21.78 $\mu m \cdot voxel^{-1}$. Stacks of section images in the welding direction/normal direction plane were then obtained after correcting the signal-to-noise ratio, the beam-hardening effects, and the ring artefacts. According to the distinction ease of material/voided regions in the WD-ND section images, the material region was then segmented for all section images by applying a threshold operation with a single gray level. An internal MATLAB code was finally used to assess the local porosity (*i.e.*, distribution, fraction, size) in the CWD-ND plane projected along the welding direction.

II.9. Fractographic analyses

Fractographic analyses of fatigue specimens were conducted using different techniques. Low-magnification observations were performed using an AmScope optical stereoscope (equipped with a CLEMEX camera) to locate crack initiation

sites and assess the surface fraction occupied by the crack propagation. Fractographic investigations were also conducted with a Hitachi SU-70 field emission gun scanning electron microscope (FEG-SEM), using secondary electron mode at 15 kV, to investigate the crack initiation mechanisms and study crack propagation leading to the final rupture of the assemblies. Energy dispersive spectroscopy (EDS) analyses were performed on fracture surfaces in order to document the chemical nature of the crack initiation site. Topographic measurements of the fracture areas were conducted with a LEXT OLS4100 laser scanning confocal microscope using a height pitch of 2 μm to position the fracture path on the 3D reconstruction volume obtained with X-ray microtomography.

II.10. Digital image correlation (DIC) technique

An ex-situ optical digital image correlation (DIC) technique was used to assess the local strain fields of the welds following the loading/unloading sequence of the specimens at various stress levels. The measured strain field corresponds to the plastic deformation due to the loading/unloading sequences, as detailed in ref.[26]. For this purpose, the CWD-ND surface was slightly gritted down with a P4000 SiC grit paper, and then etched with a Keller etchant for 30 seconds in order to produce random fine speckle at the region of interest (R.o.I.) investigated by DIC. Chemical etching for speckle pattern has the advantage not to hide and even reveal the microstructure of the welded assembly at different scales in comparison with conventional speckle techniques such as paint, and particles deposition. Besides, chemical etching for speckle has no effect on the macroscopic and local behavior of the material under monotonic tensile tests, especially for such large specimens.

Optical micrographs were taken with a DMLM LEICA optical microscope (2.5x magnification lens) in bright light mode, at a resolution of 2,452 × 2,056 pixels^2 for a field view of 4.70 × 3.94 mm^2. A total of 126 optical micrographs were manually taken with a 50% overlap in order to cover all the areas of interest (19,718 × 4,608 pixels^2, *i.e.* 37.80 × 8.83 mm^2. This imaging operation (*i.e.* taking 126 micrographs) was repeated at different steps of the interrupted tensile tests: before tensile testing (reference pictures) and after a loading/unloading sequence. Each interrupted tensile load corresponds to the maximal stress applied for a stress amplitude level tested during HCF tests. Particular care was taken to center all the micrographs with their respective reference micrographs pairs by tracking specific features in sight. Interrupted tensile tests were conducted with a MTS landmark servo-hydraulic machine.

In-plane local displacement fields were assessed for each individual micrograph region with the open source software OpenDIC developed in our laboratory by Vanderesse *et al.*[27,28]. The size of the subsets was defined at 55 x 55 pixels, i.e. 105 µm, with a regularly spaced step size of 10 pixels (19 µm). The subpixel displacement was measured with a precision of 1/64 pixel. These values were chosen in order to ensure high spatial resolution and reasonable computation time. The subsets comprised 4 to 6 gray intensity peaks, which is usually considered as sufficient for reliable measurement. The gray levels of the image were interpolated with a biquintic function. The displacement fields were filtered with a gaussian blur algorithm in order to reduce the noise over a kernel with radius 2 pixels. The smoothed displacements fields were then processed for strain derivation.Noise and artifacts in the speckle pattern could arise at high deformation levels, making sometimes subset matching not reliable. This difficulty was circumvented by measuring displacement values in an incremental mode, i.e. with each deformed step being the reference for the next deformed step. This ensured an "incremental deformation/error" ratio sufficiently high to obtain accurate and quantitative results. The strain fields ε_{XX}, ε_{XY}, and ε_{YY} (x corresponding to the loading direction) were then calculated with a Java companion application working with Fiji software[29], based on a two-dimensional iso-parametric finite element formalism, with the nodes being the center of subsets and with four Gauss bilinear interpolation points per element. The strain fields of each micrograph were then merged together to obtain the global strain fields of all the welds.

III. Results

III.1. Fatigue behavior

The fatigue results performed on the two welding configurations are presented in Fig. 3. In this HCF regime, the fatigue performance of welded joints is dependent on the welding process. The FSW configuration demonstrates a higher fatigue resistance compared than that obtained with the GMAW configuration. The fatigue strength, corresponding to the run-out condition, is approximately 25% higher for the FSW configuration than for the GMAW configuration. At a high stress amplitude (σ_a = 35 MPa), the assemblies produced by FSW process exhibit a lifespan about three times higher than that of the GMAW process.

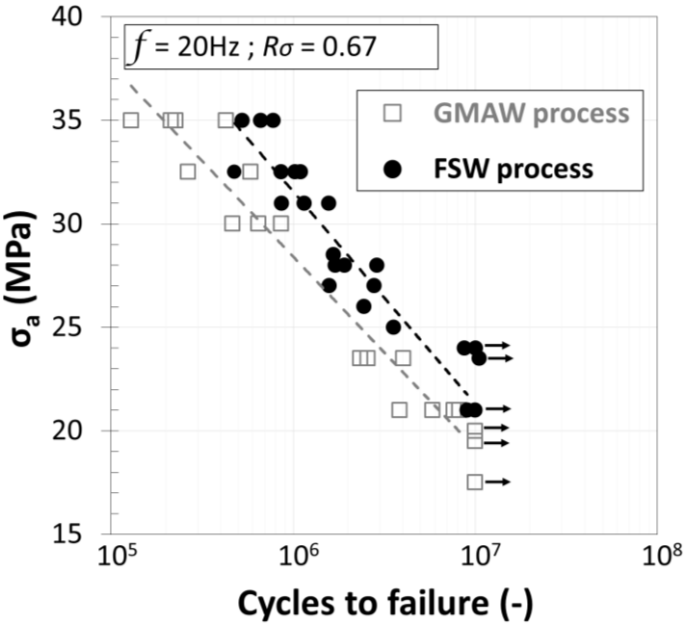

Fig. 3: S-N curves for GMAW (white marks) and FSW (black marks) welded assemblies.

III.2. Fractographic analyses

III.2.a. GMAW configuration

Low- and high-magnification observations of GMAW fractured surfaces are presented in Fig. 4. Three different crack initiation sites were found for the GMAW assemblies: i/ at the interface of pass #2/pass #3, on the top surface (represented by an orange mark in Fig. 4.a); ii/ at the interface of pass #2/HAZ, on the top surface (represented by a red mark in Fig. 4.a), and iii/ at the notch root (represented by a blue mark in Fig. 4.a). A dependence between the location of the crack initiation sites and the stress amplitude regime was observed (please see *e.g.* the colored marks in Fig. 4.a). Interestingly, crack initiation occurred at the notch root at low stress amplitude regime (*e.g.* $21 < \sigma_a < 23.5$ MPa), while crack initiation systematically occurred at the surface of the specimen in high stress amplitude regime (*e.g.* $30 < \sigma_a < 35$ MPa).

Low-magnification fracture surfaces observed via confocal microscopy (Fig. 4.b and c) revealed that cracks propagated rather perpendicularly to the loading direction, producing a relatively smooth surface (shown in light gray in Fig. 4.b and c) as compared to the final fracture surface (in dark gray in Fig. 4.b and c). The

morphology of the fatigue crack front and the presence of many river lines suggest that the macroscopic crack results from the coalescence of multiple microscopic cracks initiating from the surface and sub-surface regions, regardless of the stress amplitude regime.

As previously revealed from cross-section macrographs (Fig. 1), the GMAW joint contains a substantial volume fraction of pores, which are clearly visible on fractured surfaces (*e.g.* black dots in Fig. 4.b and c). They participate either in the fatigue crack propagation phase or in the final rupture of the fatigued specimens in high or low stress amplitude regimes, respectively. In the low stress amplitude regime, the crack initiated and propagated within the base material/HAZ at the notch root and the final fracture occurred within the third welding pass. Therefore, pores were exclusively observed in the final fracture area (upper third area on the fracture surface in Fig. 4.b). It is worth mentioning that some fretting occurring at the notch root under cyclic loading (this mechanism is further detailed in Fig. 6) weakened the structural assembly and led to failure in the region, where the base material was thermally affected by the GMAW process. High-magnification observations in a typical crack initiation site confirmed that crack initiated from a grain at the surface region in the base material (pointed by a gray arrow in Fig. 4.b, d and f). EDS analyses conducted on this crack initiation site revealed no trace of segregated elements, confirming that no inclusion was present in the material. In the high stress amplitude regime, fatigue crack initiated from fine pores ($50 < D_{pores}$ 100 µm), and was densely distributed (within an average spacing < 500 µm) at the interface of pass #2/pass #3 (Fig. 4.e and g). The nucleated crack then propagated within welding pass #2 (Fig. 4.e). Millimeter-size and densely distributed pores in the final fracture region, combined with a linear defect in the mid-section of the specimen (represented in Fig. 4.c), resulted in a decrease in the assembly toughness, contributing to the low fatigue performance of GMAW specimens.

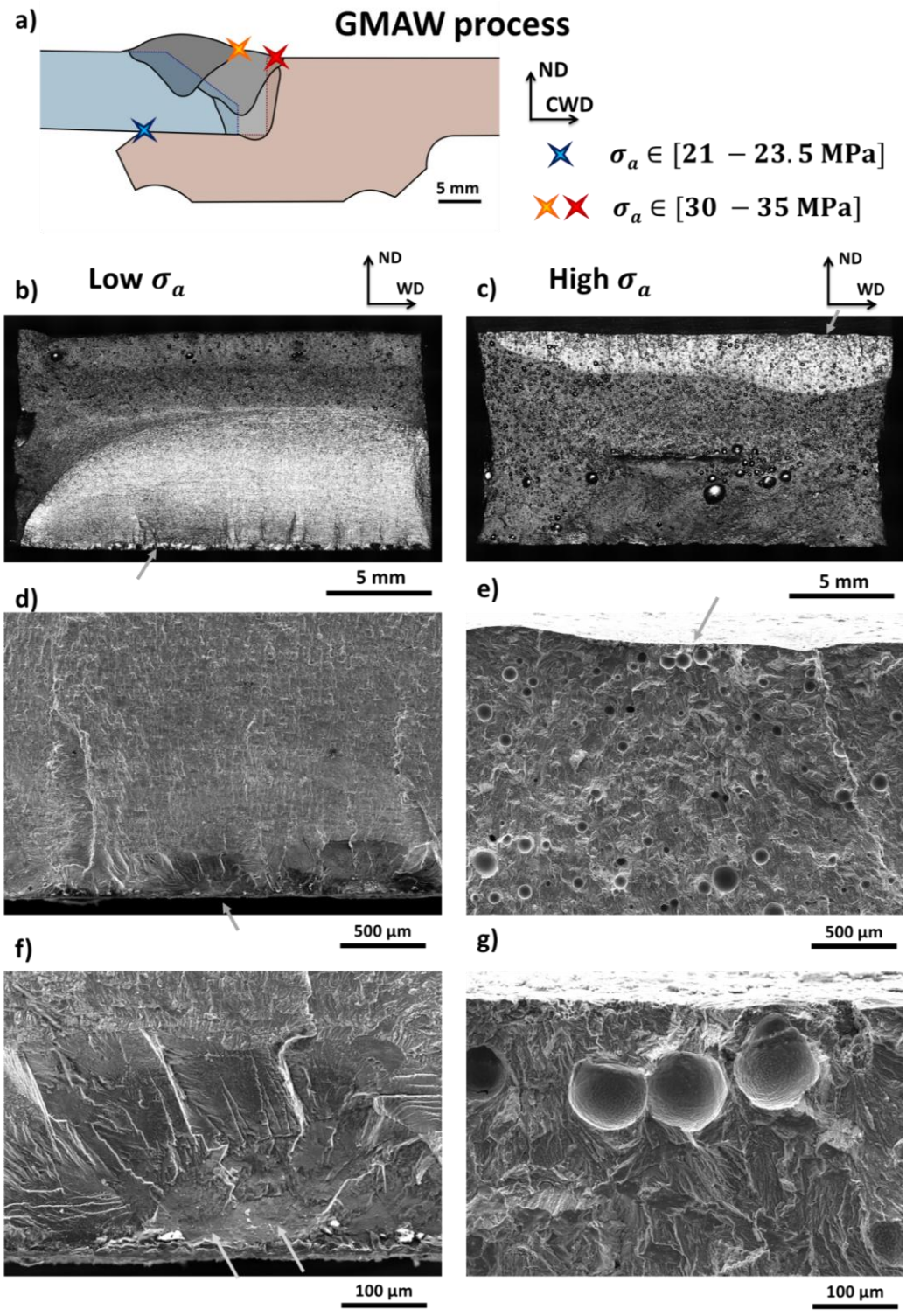

Fig. 4: Fractographic analyses of fatigued GMAW specimens showing the evolution of the crack initiation mechanism as a function of the stress amplitude regime, i.e. from grains at the notch root in the low stress amplitude regime and from pores in the pass/pass or pass/HAZ interfaces in the high stress amplitude

regime: a) schematic side view illustrating the location of the crack initiation sites reported for different stress amplitude ranges; b-c) laser confocal low-magnification observations of whole fracture surfaces for two different loading conditions; d-e-f-g) SEM high-magnification observations of the crack initiation sites for two different loading conditions . The gray arrows in Fig. 4.b to e highlight the region of interest for higher magnification observations.

III.2.b. FSW configuration

Low- and high-magnification observations of FSW fractured surfaces are presented in Fig. 5 and Fig. 7, and are used to investigate the fatigue crack initiation and propagation mechanisms. As represented in Fig. 5.a, two distinct and recurrent locations of crack initiation sites were found regardless of the stress amplitude regime for FSW assemblies: i/ at the notch root (represented by a blue mark in Fig. 5.a), and ii/ within the nugget zone (NZ) close to the TMAZ at the crown surface, on the retreating side (represented by a red mark in Fig. 5.a). Interestingly, most of the specimens failed due to a crack growing from the notch root due to a fretting mechanism similar to the one reported in GMAW configurations. Laser confocal observations of the whole fracture surface (Fig. 5.b) confirmed the coalescence of several crack initiation sites located in surface and sub-surface regions, forming a macroscopic crack leading to the final failure of the specimens. High-magnification SEM observations of crack initiation sites (Fig. 5.c and d) indicated that cracks initiated from large grains ($100 < D_{grain}$ 200 µm) in the surface or sub-surface regions.

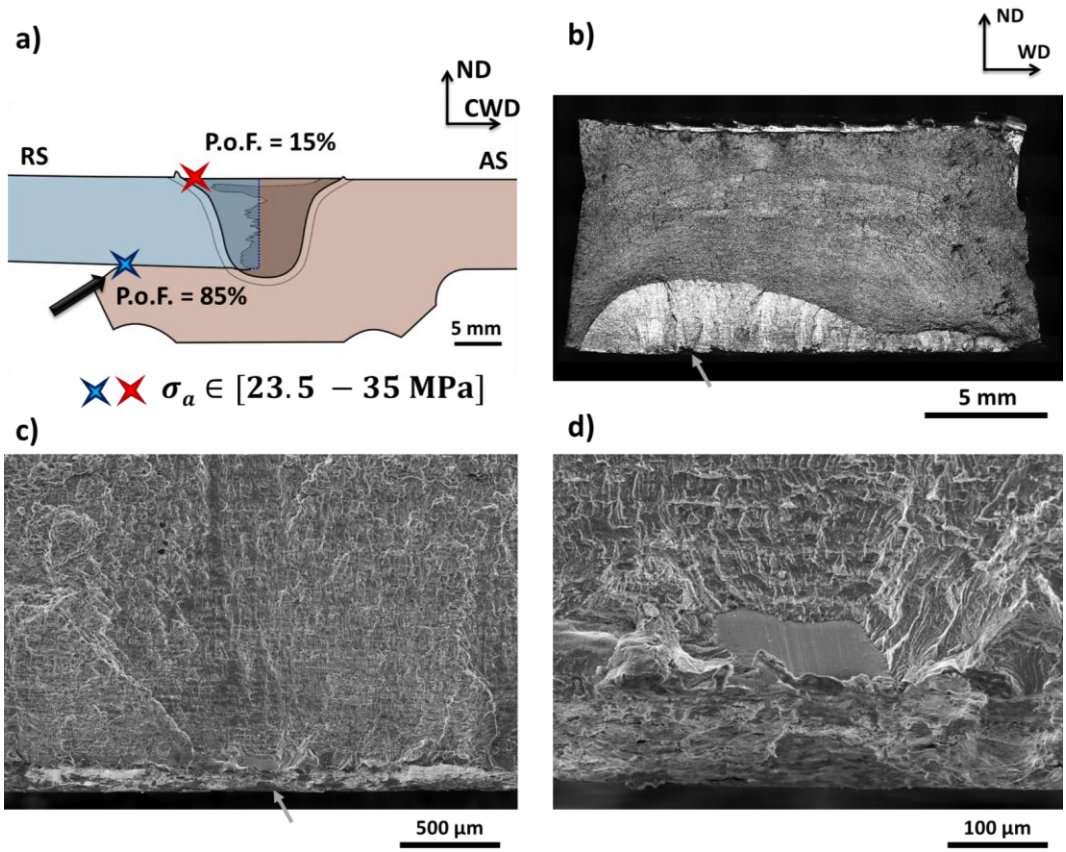

Fig. 5: Fractographic analyses of fatigued FSW specimens showing crack initiating at the notch root, i.e. the highest probability of failure scenario (P.o.F.=85%), regardless of the stress amplitude regime: a) schematic side view illustrating the location of the crack initiation sites with their respective probabilities of failure; b) laser confocal observations of the whole fracture surfaces; c-d) SEM high-magnification observations of the crack initiation sites. The gray arrows in Fig. 5.b and c highlight the region of interest for higher magnification observations.

Complementary observations of one typical crack initiation site at the notch root of FSW specimens displayed a contact area produced by an intense and repetitive contact fretting occurring during fatigue testing (Fig. 6). In some instances, material chips were seen at the notch root, confirming the severity of the contact. In the vicinity of the fracture surface, material beads resulting from the accumulation and spreading of material debris due to cyclic stresses were also clearly visible. Horizontal streaks aligned with the loading direction (Fig. 6.c) were observed in the

material bead region, while extrusion streaks were shown to be vertical (Fig. 6.b). This observation confirms that repetitive contact and friction (repeated relative tangential displacement of the two parts in contact of 400 µm approximatively) are taking place in this region. Secondary cracks were also observed in the material bead regions (white arrows in Fig. 6.c).

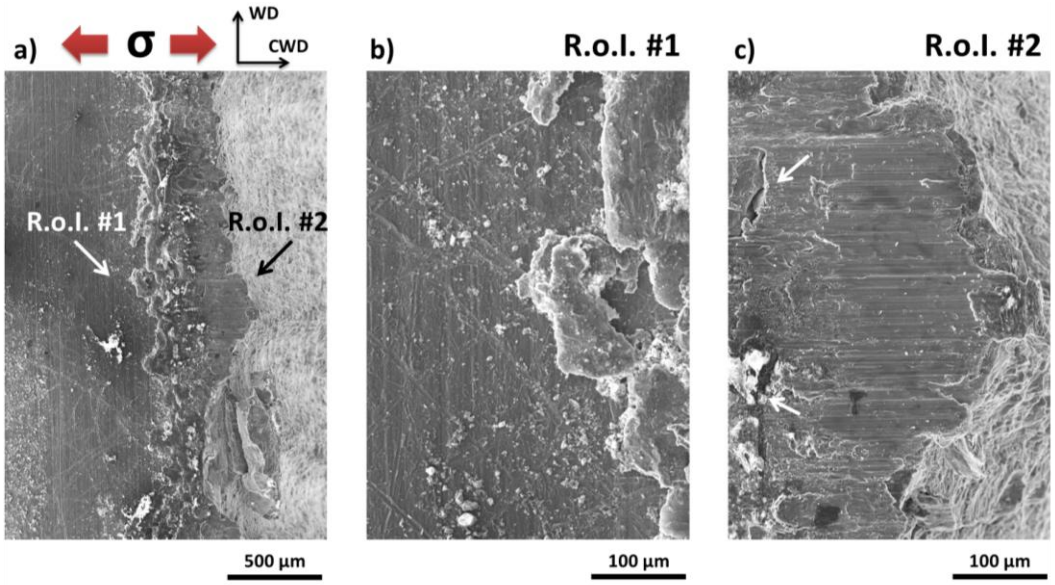

Fig. 6: SEM observation of fatigued FSW specimen in the normal direction (ND) showing a contact and friction region near the fracture surface at the notch root (P.O.F.=85%): a) macroscopic view of a fatigue-tested specimen showing both the vertical extrusion streaks (R.o.I. #1) and horizontal streaks in the material bead region due to friction (R.o.I. #2); b-c) micrographs in two regions of interest (R.o.I.) illustrating the vertical extrusion streaks due to friction.

As mentioned above, for FSW specimens, fatigue crack also initiated from a less recurring site (P.o.F.= 15%) located within the nugget zone (NZ) close to the TMAZ, at the crown surface, on the retreating side (represented by a red mark in Fig. 7.a). Some periodicity in the initiation and propagation phases can be seen on the fracture surface. These cracks coalesce to form the macroscopic fatigue crack (Fig. 7.b and c). Interestingly, the periodicity of the crack initiation and propagation features seems to correspond to that of the striated pattern (crown surface) induced during the FSW process (*i.e.* corresponding to the advancement of the FSW tool for one revolution). Although the crack propagation paths were clearly identified on the fracture surface with river lines (Fig. 7.d), finding the crack initiation sites was almost impossible due to the small fractographic features related to the micrometer-

size grains and an apparent intergranular crack mechanism visible in Fig. 7.e. It is worth mentioning that all the fatigued specimens with a P.o.F. of 15% also presented secondary cracks in the contact region, at the notch root (Fig. 7.f and g). In this respect, damage features related to one-off folding/bending are visible on the specimen side in the region where secondary cracks were formed (Fig. 7.f). The black dashed lines in Fig. 7.f and g aim to identify the location of the one-off folding/bending region and the secondary cracks.

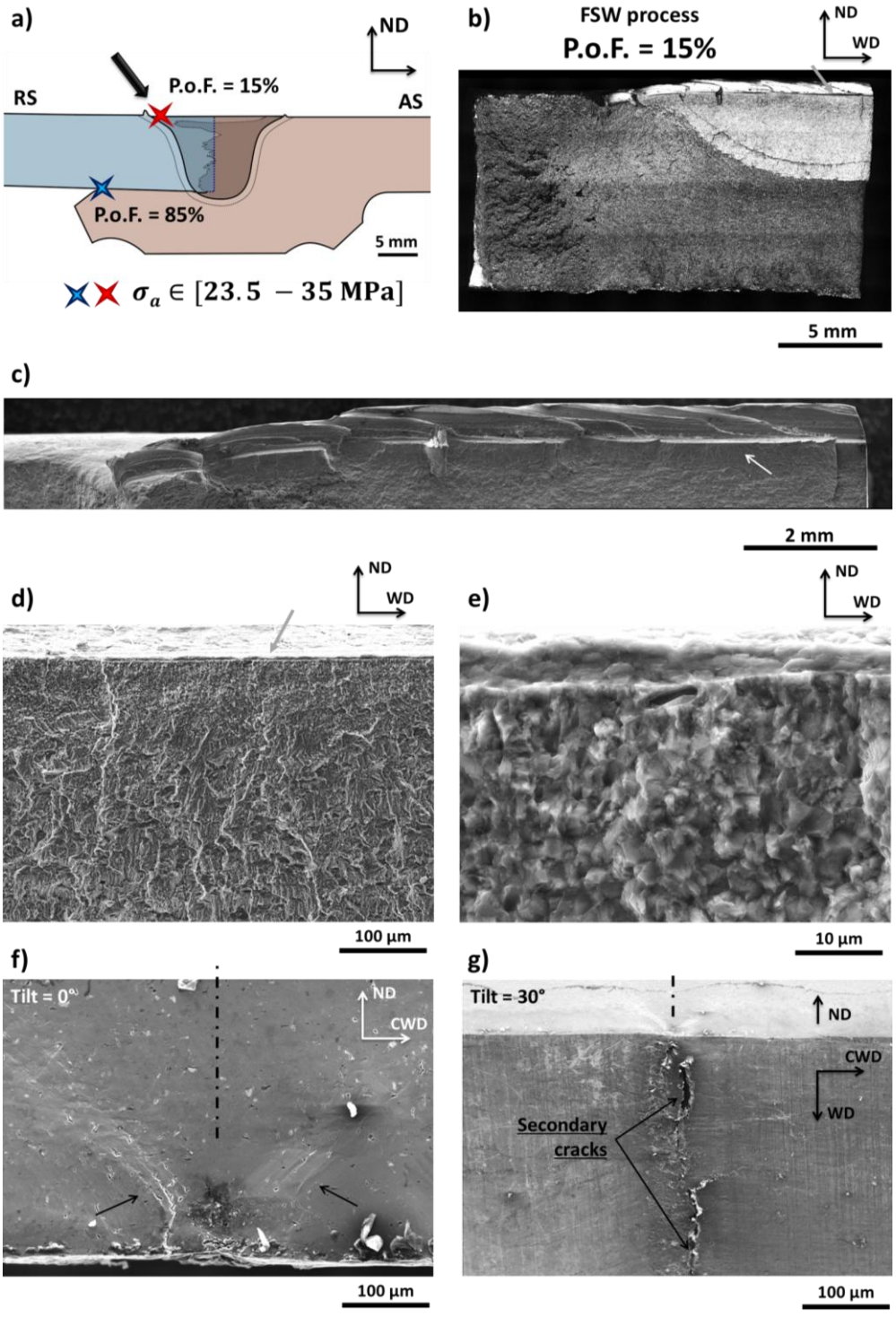

Fig. 7: Fractographic analyses of fatigued FSW specimens failing from a crack initiating within the nugget zone (NZ) close to the TMAZ at the top surface on the retreating side, i.e. the lowest probability of failure scenario (P.o.F.=15%), regardless of the stress amplitude regime, and the occurrence of secondary cracks: a) schematic side view illustrating the location of the crack initiation sites

with their respective probability of failure; b) laser confocal observations of the whole fracture surfaces; c-e) SEM observations of the crack initiation and crack propagation region showing the multiple periodic crack initiation sites; f-g) SEM observations of secondary cracks formed at the notch root for all FSW specimens with crack nucleated from the top surface. The gray arrows in Fig. 7.b to d highlight the region of interest for higher magnification observations. The black dashed lines in Fig. 7.f and g aim to clarify the location of the one-off folding/bending region and the secondary cracks.

III.3. Tomographic and topographic analyses

X-ray tomographic characterizations were conducted on GMAW and FSW configurations to assess the occurrence and distribution of defects within the welded joints. No defects (*i.e.* porosities, lack of penetration or tunneling defects), were probed for the FSW configuration. A representation of the average of all tomographic slices obtained for the whole GMAW projected along the welding direction (WD) is depicted in Fig. 8. This 2D projection of the whole specimen aimed to quantify the occurrence of micrometer- and millimeter-size pores previously found in Fig. 4. Proceeding from welding pass #1 to pass #3, the area fraction of pores progressively decreased (f = 2.7% > = 2.1% <> = 1.4%). However, the size of the pores increased. Pores were found within the whole first welding pass and in the periphery of pass #2 and pass #3, while larger pores were found in pass #2 and pass #3. In particular, a high area fraction of pores was found at the top surface weld toe, at the interface of pass #2/pass #3 (f = 8.5% at the weld toe) and at the interface of pass #2/HAZ (f = 5.3% at the weld toe). Moreover, optical microscopy revealed a continuous defect region (fine pores, pointed by a white arrow in Fig. 8) in the middle section of the assembly at the interface of pass #2/HAZ. The initiation site from the top surface (orange mark in Fig. 8) and the typical fatigue crack path (dashed orange line in Fig. 8) in the high stress amplitude regime were superimposed on the porosity map. They correspond well to regions with high densities of pores and confirm the significant contribution of these weld defects to the crack initiation (interface between pass #2 and pass #3) and propagation phase (upper region of pass #2). The final crack path (dashed red line in Fig. 8) also highlighted the influence of the porosity on the toughness of the GMAW specimen.

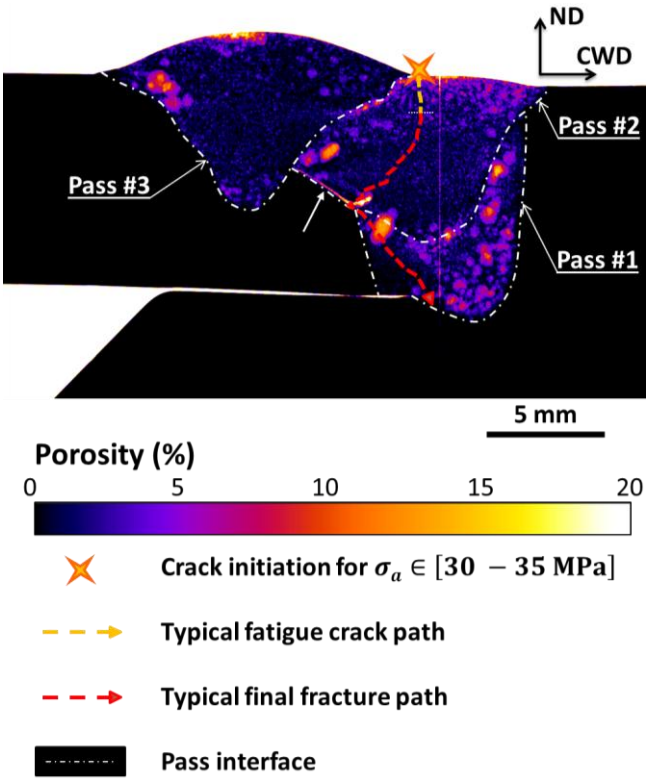

Fig. 8: Representation of the porosity distribution of a GMAW assembly in the CWD-ND plane obtained by X-ray microtomography analyses. The evolution of the porosity from pass to pass and location of large pores in the periphery of passes was evidenced. A continuous defect region highlighted with a white arrow was found in the mid-section of the joint assembly at the interface of pass #2/HAZ. The crack path of a fatigue-tested specimen in the high stress amplitude regime obtained via confocal microscopy was reported on the porosity distribution (green dashed line). The crack initiated at the interface of pass #2/pass #3 at the top surface of the specimen.

III.4. Local mechanical properties characterization via micro-indentation technique

The profile obtained at the center of the specimen is presented in Fig. 9. The typical regions of welded assemblies were identified, including the fusion zone (FZ), the heat-affected zone (HAZ), and the base material (BM) for the GMAW configuration (white plot), as well as the nugget zone (NZ), the heat-affected zone (HAZ), the thermo-mechanically affected zone (TMAZ), and the base material (BM) for the FSW configuration (black plot). A maximum hardness value of about 95 ± 3HV was obtained in the base material region, while the local properties of the joint in the HAZ, FZ and HAZ, TMAZ, NZ regions (*i.e.* from either side of the base material) significantly dropped down to 61 HV and 64 HV for the GMAW and FSW configurations, respectively. These HAZ and TMAZ regions extend to

about 10 mm (slightly larger for the GMAW configuration) on either side of the assemblies and clearly demonstrate a low hardness. The GMAW welding sequence produced a structural assembly with heterogeneous local hardness along the middle section, including the HAZ/FZ/HAZ/FZ/HAZ regions.

For the FSW configuration (Fig. 9), the hardness increased from 64 HV in the HAZ to 92 HV in the TMAZ, region on the retreating side, and to 82 HV on the advancing side. There were some variations in hardness in the NZ, as it gradually decreased from the retreating side to the advancing side in the upper section of the assembly and became significantly constant along CWD in the middle and bottom sections of the assembly. Finally, local mechanical properties were much higher in the NZ for the FSW configuration than they were for the FZ for the GMAW configuration.

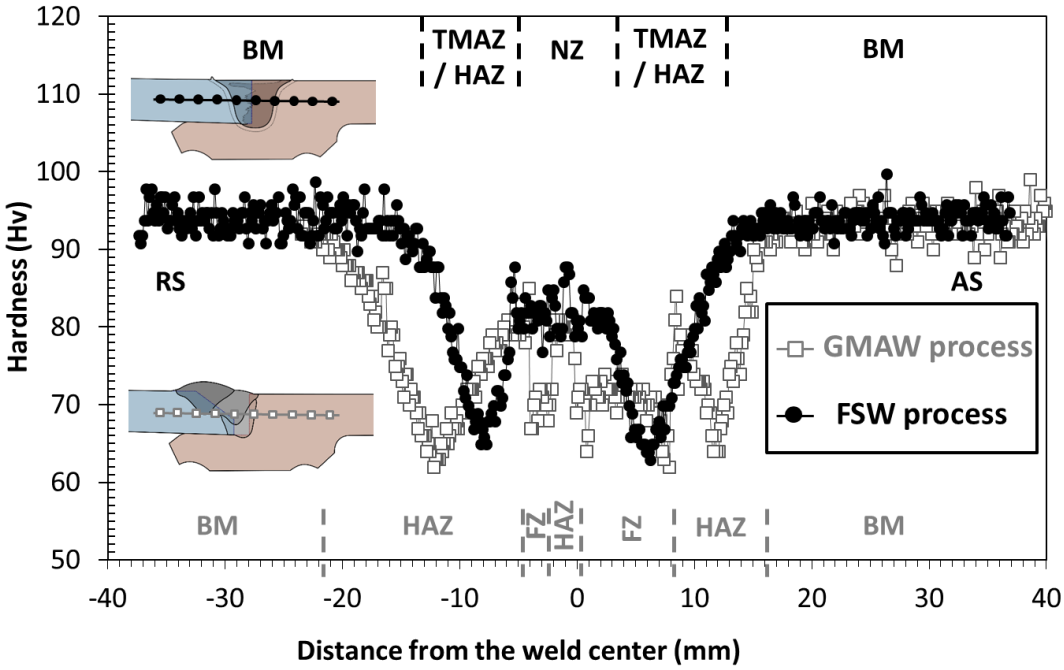

Fig. 9: Microhardness profiles for the GMAW and the FSW configurations measured at the center of the specimen along the cross-welding direction in order to document the local heterogeneous mechanical behavior of the weld assemblies. Typical regions were highlighted, i.e. the fusion zone (FZ), the heat-affected zone (HAZ) and the base material (BM) for the GMAW configuration, and the nugget zone (NZ), the heat-affected zone (HAZ), the thermo-mechanically affected zone (TMAZ) and the base material (BM) for the FSW configuration. The advancing side (AS) and retreating side (RS) are reported on the graph for the FSW configuration.

III.5. Local strain field characterization via optical digital image correlation technique

Ex-situ digital image correlation (DIC) tests were conducted on GMAW and FSW configurations to assess the local plastic strain fields of the welded assemblies subjected to a mechanical loading (Fig. 10 and Fig. 12). As aforementioned, the local strain was evaluated after incremental loading up to specific loads and unloading. In this respect, local deformations calculated from the displacement measurements correspond to the irreversible local plastic deformation after specified axial loadings. Strain fields measured in the principal direction strain component ε_{XX} and in the shear strain component ε_{XY} are reported in Fig. 10 and Fig. 12. Cold and hot colors for ε_{XX} correspond to non-deformed and highly deformed regions (*i.e.*, 0.0% [blue] < ε_{XX} < 4.5% [yellow]), respectively, whereas cold and hot colors for ε_{XY} both correspond to highly deformed regions, while local non-deformed regions are depicted in orange. The DIC technique was successfully used in this study to demonstrate how the local strain fields were very heterogeneous and sensitive to local microstructural features and defects.

III.5.a. Local strain assessment for GMAW configuration

For the GMAW configuration, the yielding was localized within welding passes #2 and #3, even at the first loading step, *i.e.* 81 MPa, especially in the vicinity of the welding pass interfaces (white arrow in Fig. 10 for ε_{XX} at 81 MPa and 106 MPa). At this stress level, the permanent deformation measured outside the joint was almost equal to 0%, confirming the elastic behavior of the assembly in this loading regime. The strain localized first within the different weld passes (*i.e.*,), while three maximal strain sites can be found (these high deformation spots are especially visible for high stress levels in Fig. 10) at the bottom region of pass #3, at the interface of pass #2/pass #3, and at the interface of pass #2/HAZ (as indicated by black arrows in Fig. 10 at 182 MPa). As the applied stress increases, the strain increases faster in the regions that show strain localization than in the whole specimen. Intense strain localization was also visible on the ε_{XY} strain fields in the welding pass periphery, corresponding to where large pore sizes, high pore volume fractions, and a continuous defect region (fine pores) were found via X-ray tomography analyses (see Fig. 8) or the HAZ region highlighted via microhardness. A significant out-of-plane deformation of the top region of the specimen surface produced rounded and thus unfocused regions, disabling the strain distribution to be quantified within a region about 100-250 µm wide. For the same reason, the intensity of the strain localization at the interface of pass #3/pass #2, or at the interface of pass #2/HAZ, while significant, was probably

underestimated in Fig. 10, particularly in the vicinity of the crack initiation sites (as represented by red and orange marks in Fig. 4.a). At high stress levels, there was significant deformation at the notch tip and the notch root, the latter region being a crack initiation site in the low stress amplitude regime (as represented by a blue mark in Fig. 4.a).

A combination of the DIC technique with optical observations of the specimen after the first loading step (*i.e.* loading up to 81 MPa, and then unloading) particularly highlight the contact of the base material at the notch root in the low stress amplitude regime (Fig. 11). The notch, slightly open prior to mechanical testing (Fig. 1.b and Fig. 8), progressively closed up and witnessed the contact at the notch root after a loading/unloading as low as 81 MPa (white arrow in Fig. 11.a and b). The relative normal displacement $\Delta V/D$ (where $\Delta V = V_1 - V_2$) from the upper and bottom sides of the notch in comparison to the state prior to mechanical loading is plotted over a specific length in Fig. 11.d to quantify the contact phenomenon after various loading steps. Each measurement of the profile corresponds to the relative displacement of two subsets symmetrically chosen from the notch up to 0.5 mm (D = 1.0 mm). At low stress levels (81 MPa), the contact region is clearly visible on the micrograph (white arrow in Fig. 11.a and b), while the positive relative displacement reported in Fig. 11.e confirms that the notch opens slightly ($\Delta V/D > 0\%$). It is worth mentioning that fatigue testing performed on the GMAW specimens up to this low stress level have an equivalent amplitude of σ_a = 20 MPa and lead to run-out results (more than 10^7 cycles). For higher maximum stress levels ($\geq$ 106 MPa), the closure of the notch is possible ($\Delta V/D < 0\%$), leading to local compression and contact of surfaces. The intensity of the compression in this region increases with the external stress level. Note that for all stress levels higher than 106 MPa, the relative displacement in this region is always negative over the control length, demonstrating a contact all along the notch, with a higher compression intensity at the notch root.

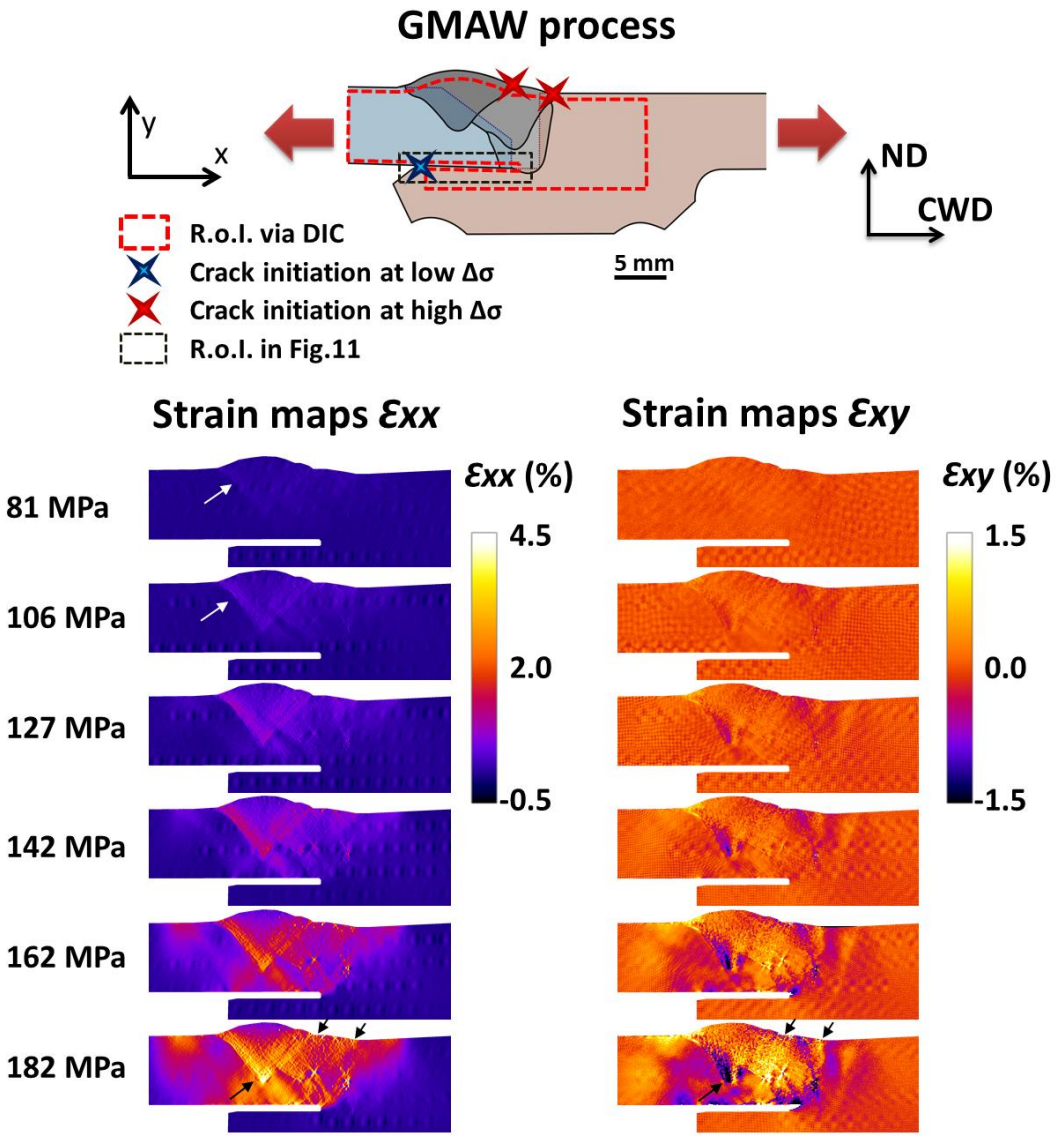

Fig. 10: Schematic illustration of the region of interest for DIC experiments performed on the GMAW configuration and strain maps (ε_{XX} and ε_{XY}) for different loading conditions. Strain localization occurred near the pass interfaces, within pass #3, in the high porosity regions of the weld passes, in the HAZ, and at the notch root depicted by black arrows for the 182 MPa loading condition.

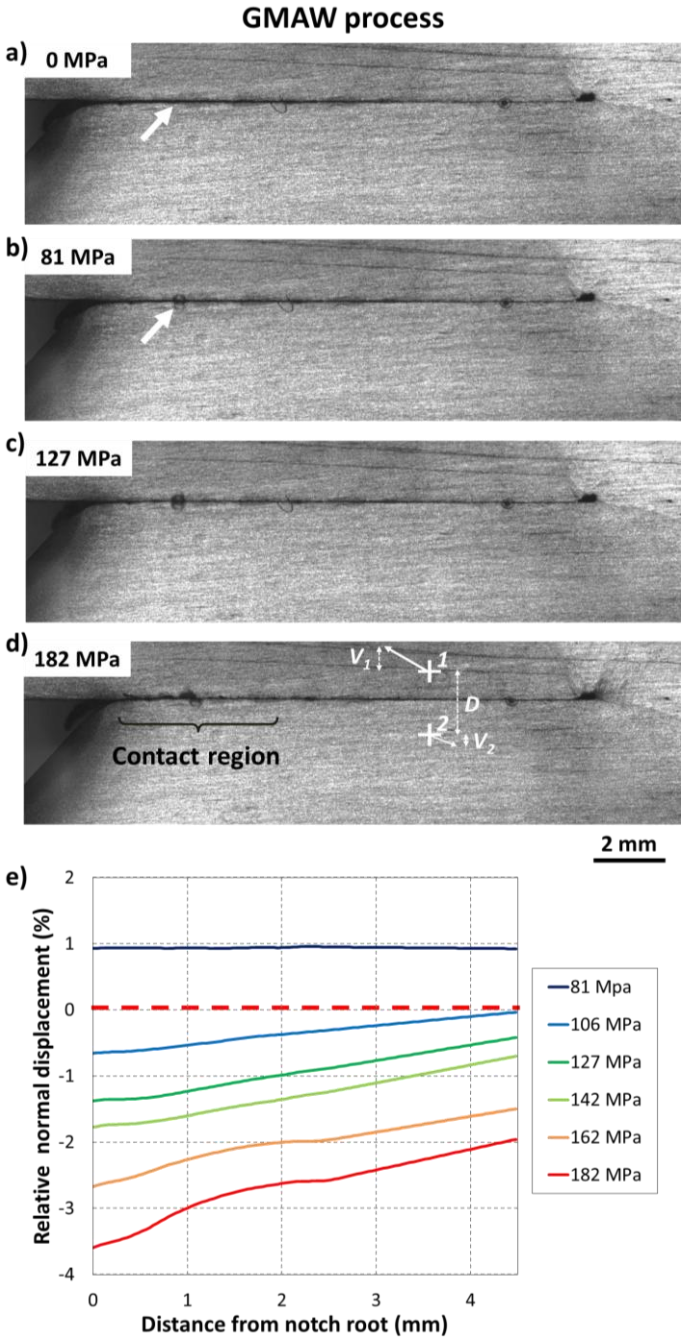

Fig. 11: Optical micrograph GMAW configurations showing evidence of the contact region occurring at different stress levels at the notch root (the R.o.I. is presented as a black dashed box in the schematic illustration in Fig. 10): a) 0 MPa, b) 81 MPa, c) 127 MPa, and d) 182 MPa; e) Evolution of the relative displacement ΔV/D in the contact region showing the compression state due to

loading. The region of interest (black bracket) and the definition of the relative normal displacement $\Delta V/D$ (where $\Delta V = V_1 - V_2$) along the normal direction (ND) are presented in Fig. 11.d.

III.5.b. Local strain assessment for FSW configuration

Similar DIC examinations were conducted for the FSW configuration (Fig. 12). As shown in Fig. 12 (at 109 MPa), the onset of plasticity first starts in the HAZ on both sides of the welded joint, with the strain intensity being slightly higher on the retreating side. Indeed, two inclined strain localization bands (*i.e.* bands parallel to the interface of the TMAZ/NZ) are clearly visible on the deformation maps presented in Fig. 12. The polarity inversion of the ε_{XY} strain field on the retreating side and on the advancing side bands (cold versus hot colors in Fig. 12, respectively displayed as white arrows at 109 MPa) demonstrates the opposite displacement of the nugget zone along the ND in comparison with the base material due to shearing. This displacement along the ND participates in the contact occurring locally in the vicinity of the notch root (Fig. 13). As the applied stress increases, strain localization increases more significantly on the retreating side. As shown in Fig. 12, plasticity occurred at other locations of the assembly for higher loading conditions. Intense strain localizations near the top surface within the nugget near the TMAZ on the advancing and retreating sides were found for loadings up to 163 MPa (Fig. 12). These regions were identified as a potential crack initiation sites (as previously seen in Fig. 7 for P.o.F. = 15%).

Similarly to the GMAW configuration, the contact region in the notch root (associated with a high-potential crack initiation site for the FSW configuration in this loading range (see Fig. 5 for P.o.F. = 85%) was examined to quantify the relative normal displacement along the ND from both sides of the notch (Fig. 13). At low stress levels (109 MPa), contact at the notch root was observed on micrographs (white arrows in Fig. 13.a and b, but no relative displacement was recorded ($\Delta V/D \approx 0\%$ *in* Fig. 13.e)). The compression contact region was increasingly visible as the stress level increased to 172 MPa, after which it stabilized ($\Delta V/D < 0\%$ in Fig. 13.e). Conversely to the GMAW configuration (Fig. 11.e), the relative displacement along the notch (*i.e.* the distance over the control length) measured for the FSW configuration is not always negative (Fig. 13.e). Indeed, the deformation profile along the ND indicates a compression state in the contact region (*i.e.* a negative relative displacement reported in Fig. 13.e between 0 to 3 mm) and an opening of the notch a few millimeters aside from the contact

location (*i.e.* positive relative displacement reported in Fig. 13.e for distances > 3 mm). This leads to bending stresses along the notch and to an intense one-off contact.

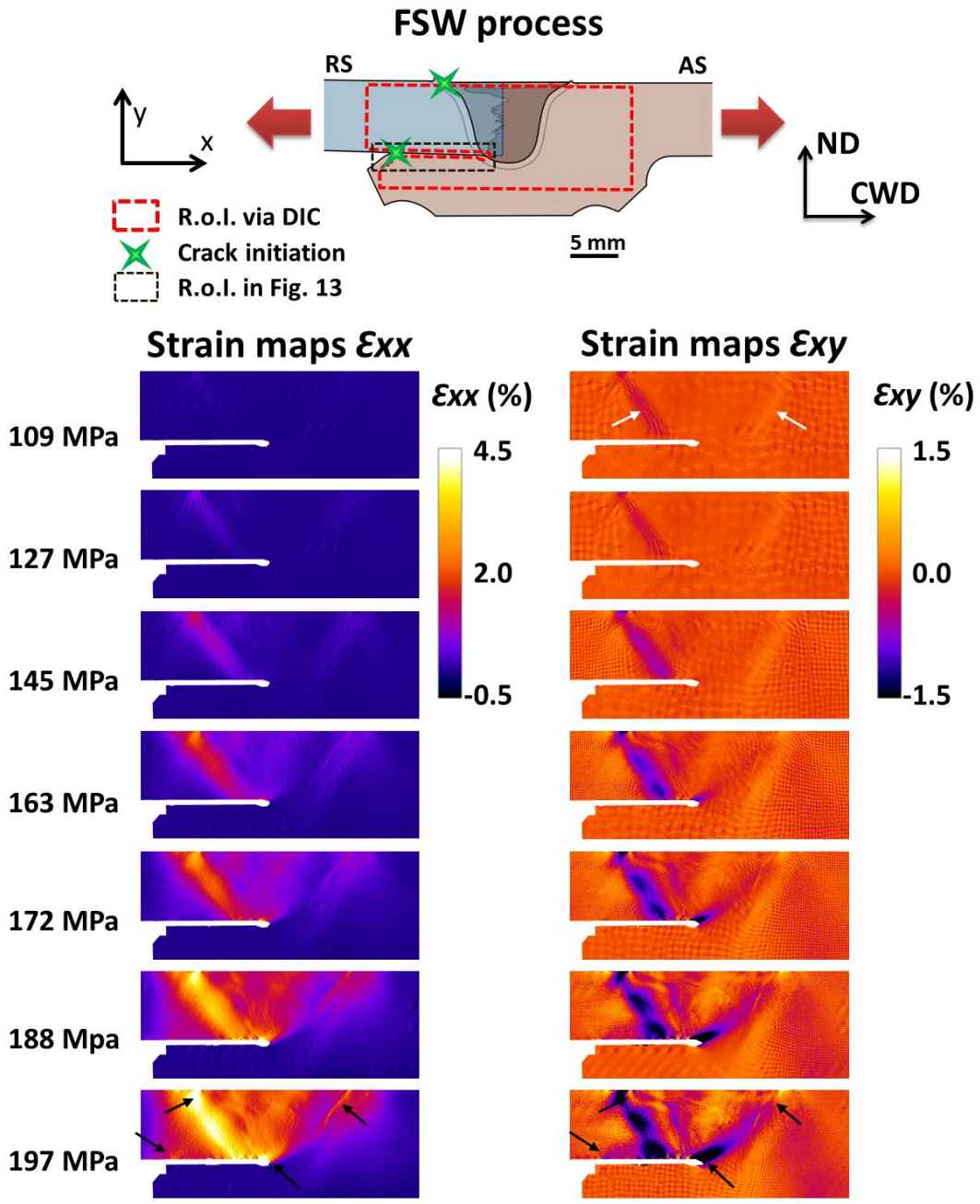

Fig. 12: Schematic illustration of the region of interest for DIC experiments performed on the FSW configuration and strain maps (ε_{XX} and ε_{XY}) for different loading conditions. Strain localization occurred in the HAZ on both sides of the

nugget zone, within the nugget region, at the notch root and at the notch tip depicted by black arrows for the 197 MPa loading condition.

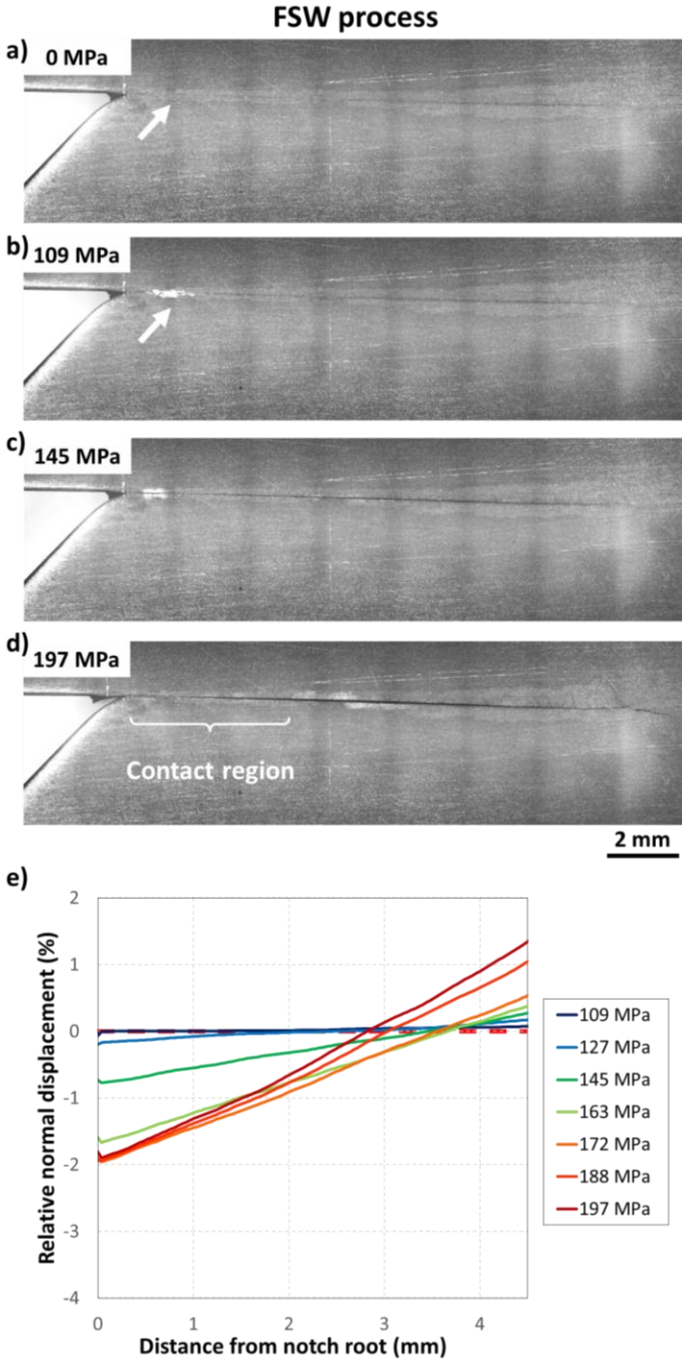

Fig. 13: Optical micrograph FSW configurations showing evidence of the contact region occurring at different stress levels at the notch root: a) 0 MPa, b) 109 MPa, c) 145 MPa, and d) 197 MPa; e) evolution of the relative normal

displacement ΔV/D in the contact region showing the compression state due to loading. The region of interest (white bracket) and the definition of the relative normal displacement ΔV/D (where $\Delta V = V_1 - V_2$) along the normal direction (ND) are presented in Fig. 13.d.

III.5.c. Relative tangential displacement assessment at the contact point

The fretting phenomenon has been investigated more in details using DIC technique for measuring the relative tangential displacement at the contact point after a monotonic loading then unloading for several loading conditions (Fig. 14.a). This relative tangential displacement is mostly due to the plasticity of the welded region during the first cycle (as depicted in Fig. 10 and Fig. 12). However, this displacement is not representative of the repeated relative tangential displacement when cycling with a load ration of R_σ=0.67, this latter repeated displacement not being quantitatively measured in the present study. In addition, it is worth noting that the sliding direction in the contact region can be observed on the surface of the specimen due to the occurrence of wear particles compaction solely on one side of the friction area (Fig. 14.b). Interestingly, this sliding direction corresponds to the relative displacement from the upper and bottom sides of the notch during the unloading phase when fatigue testing. The progressive blurring of the vertical streaks in the vicinity of the friction zone (at the beginning of the sliding) also informed on the progressive contact pressure experienced.

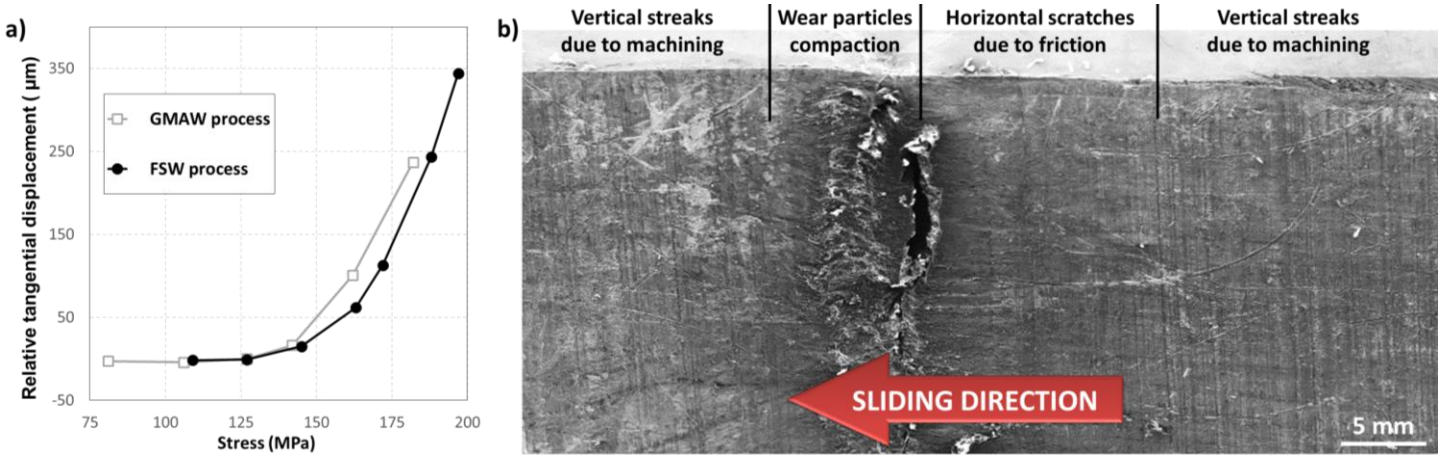

Fig. 14: a) Evolution of the relative tangential displacement at the contact point after a monotonic loading then unloading, i.e. the first cycle during fatigue testing, b) Observation of the contact region highlighting the sliding direction due to structural-contact-fretting (contact region with friction and wear particles compaction at the end of the sliding movement).

IV. Discussion

The present investigation distinguished itself from previous research by tackling a more intricate welding configuration (versus conventional butt or overlapped configurations) using a permanent backing plate required by the railway industry for positioning and alignment purposes. The design of the present welding configuration was shown to impair the fatigue performance of the welded assemblies, generating an unforeseen local and repetitive compression (few percent compressive strain) and friction at the notch root due to out-of-plane deformation along the ND and notch closure effects under cyclic loading for the two welding configurations (Fig. 11 and Fig. 13). This local compression along few millimeters (Fig. 11.e and Fig. 13.e).) and local relative tangential displacement (< 500 µm in Fig. 6 and Fig. 14) lead to structural-contact-fretting crack initiation mechanisms, which in turn lead to transgranular cracking mechanisms of surface/sub-surface grain (Fig. 4.b, d, and f, Fig. 5, and Fig. 6). The contact region is much longer than the repeated relative tangential displacement (Ratio < 500 µm/2.8 mm = 0.18), and thus correspond to mode I fretting mode, i.e. sliding wear[30–32]. According to the wear particles compaction solely on one side and scratches due to friction, it is possible to identify a sliding whose direction refers to the unloading phase when fatigue testing (small oscillations in the contact region). It is thus believed that the notch opened then closed up to contact then friction at the notch root during the loading then unloading sequence, respectively. The structural-contact-fretting was thus the result of structural deformation of the welded assembly. To the authors's knowledge, such a structural-contact-fretting crack initiation mechanism has not been reported in the literature.

Concomitant cracks initiating from typical welding defects also participate in the failure process of the welded assemblies subjected to cyclic loading (Fig. 4.c, e and g, and Fig. 7). Fine and densely distributed pores located in the weld toe region, *i.e.* at the interface of pass/HAZ, were found to favor crack initiation for the GMAWed assemblies (Fig. 8). The occurrence of such fatigue crack initiation sites were previously reported by Moreira *et al.*[9] and da Silva *et al.*[14] with respect to AA6XXX-T6 butt-GMAWed assemblies. The authors attribute such failure mechanisms to the higher porosity in weld toe region as compared to the whole weld pass, a lack of wetting, and the geometrical curvature due to filler material reinforcement, which cause high stress concentrations in this specific region. In addition, the relative low mechanical properties within HAZ (confirmed by

microhardness measurements) and the sharp transition in hardness properties in the FZ/HAZ transition region demonstrate a softening character leading to an intense strain localization within this particular region following mechanical loading (Fig. 10). The softening of these regions is usually ascribed to phase transformations occurring as a consequence of the thermal cycle experienced during the welding operation (in the present case, the reversion of the original β" strengthening precipitates). The DIC characterization technique was particularly successful at quantifying the local strain in the weld toe region, hence confirming the noticeable plastic deformation of these regions under monotonic testing (Fig. 10). The same regions can potentially demonstrate intensive cyclic plastic straining during fatigue testing. For the FSW process, crack initiation was found to occasionally occur from aggregates of micrometer-size grains near the limit of the tool shoulder, on the crown side of the FSWed assembly, with crack initiation sites periodically spaced from the revolutionary pitch (Fig. 7). Conventional butt FSWed assemblies made of AA6XXX-T6 plates were previously reported to fail from this particular region as well[9,21]. The DIC technique demonstrates its capacity to identify all the soft regions in the weld assembly that are potential crack initiation sites under fatigue conditions due to intense plastic strain localization. Such intense plastic strains have previously been reported in the literature as developing close to the boundaries of the tool shoulder, on the crown side, under monotonic tensile[22] and cyclic stresses[23] for FSW assemblies. To the authors' knowledge, no experimental findings on strain localization for GMAW assemblies have been reported in the literature. The DIC technique was shown capable to sound regions susceptible to fatigue crack initiation solely with monotonic tensile testing focusing on strain localization.

With complex joint assemblies, the microstructural state and structural-contact-fretting mechanisms compete for the crack initiation and macroscopic failure of the welds. Interestingly, the two welding configurations did not demonstrate the same sensitivity to these two failure mechanisms. The origin of the fatigue crack was found to be independent of the loading level for the FSWed assemblies, while being strongly sensitive to the stress amplitude level for GMAWed assemblies. For the FSWed, most of the specimens (irrespective of the stress amplitude) failed due to the structural-contact-fretting (Fig. 5, Fig. 6, and Fig. 7); some crack initiation taking place near the limit of the tool shoulder, on the crown side. The structural-contact-fretting failure mechanism was effective only for low stress amplitude regimes (*i.e.* where there was crack initiation from the notch root) for GMAWed assemblies (Fig. 4). In turn, crack initiation in the high stress amplitude regime for

GMAWed assemblies was driven by the microstructural state of the joints, and its discontinuities, in particular (Fig. 4). The predominance of crack initiation in the root of the weld only for low stress amplitudes in the case of GMAW process due to structural-contact-fretting was identified, whereas in the case of the FSW process this mode of initiation occurs more frequently regardless of the applied stress level. This phenomenon has been characterized for the first time in welded structural assemblies, to the best of the authors' knowledge. A particular attention will be paid in further researches to better understand the impact of the welding processes on the distortion, the fretting and thus the occurrence of such crack initiations at several stress levels.

The intensity of the compression contact measured via the DIC technique was higher for the GMAWed assemblies (Fig. 11 versus Fig. 13), resulting in lower fatigue properties at low stress levels. In addition, an intense strain localization was also found in the weld toe region of the GMAW joints under static loading (Fig. 10). As previously described by Besel *et al.*[23], such cyclic plastic strain regions have been shown to favor the formation of cracks in structural aluminum alloys under fatigue conditions. The DIC technique was thus a reliable technique for predicting sensitive crack initiating sites under cyclic conditions using monotonic tests coupled with DIC measurements.

V. Conclusions

The high-cycle fatigue performance of GMAWed and FSWed structural assemblies made of extruded AA6061-T6 having a permanent backing plate was investigated in the 10^5-10^7 cycle fatigue life range. Using fractographic analysis, metallographic analysis, x-ray microtomography, microhardness, and the digital image correlation technique, it was possible to identify the competition between microstructurally driven and structurally driven crack initiation mechanisms. A combined microstructural investigation using laser scanning confocal microscopy and X-ray microtomography allowed the documentation of the effect of welding defects on crack initiation and propagation phases when microstructural crack initiation mechanism is predominant. Microhardness measurements and DIC characterization during tensile loading were also coupled to highlight repetitive surface contacts and fretting in a softened region at the notch root (*i.e.* due to the permanent backing plate) leading to structurally driven fatigue crack initiation. The present

investigation allowed us to reach a few conclusions, which are summarized as follows:

1/ FSWed assemblies exhibited similar ultimate tensile strength, but slightly higher yield strength, as compared to the GMAWed assemblies. However, FSWed assemblies demonstrated significantly higher fatigue performance than GMAWed assemblies due to the absence of microstructural discontinuities (porosity) in the former. The fatigue strength corresponding to the run-out condition (*i.e.*, 10^7 cycles) for the FSW configuration was evaluated to be 20% higher than that obtained for the GMAW configuration (*i.e.* $\sigma_{a,at\,runout}^{FSW} / \sigma_{a,at\,runout}^{GMAW}$ = 24 MPa / 20 MPa). At high stress amplitudes (*i.e.* σ_a = 35 MPa), the assemblies produced by FSW have a lifespan about three times higher than those produced by GMAW.

2/ Two competitive crack initiation mechanisms were found for the two welded assemblies: a microstructural crack initiation mechanism and a structural-contact-fretting crack initiation mechanism. On the one hand, crack initiation mechanisms were found to be independent of the stress amplitude for FSWed assemblies, and on the other hand, for GMAWed assemblies, fatigue cracks were found to initiate from sub-surface grains at the notch root in the low stress amplitude fatigue regime and from pores located in the weld toe, *i.e.* at the interface of weld pass/HAZ, in the high stress amplitude fatigue regime. The unavoidable geometric curvature of the weld bead in the weld toe region for the GMAWed assemblies contributed to a higher local stress concentration than for the FSWed assemblies. For the FSWed assemblies fatigue-tested in this stress amplitude range, fatigue crack initiation from sub-surface grains at the notch root was the most representative crack initiation mechanism.

3/ For the GMAWed assemblies, the complex pore distribution certainly affected the overall toughness of the weld. The DIC technique highlighted intense strain localizations in those high porosity regions during the mechanical loading of the assemblies. For the FSWed, the same technique showed that the HAZ region evidenced via microhardness measurements on the retreating side was particularly prone to intense strain localization after uniaxial loading.

4/ The DIC technique was also particularly useful in highlighting the compressive state and the fretting stresses at the notch root during mechanical loading for both welding processes. Interestingly, planar contact and punctual contact were identified at the notch root for the GMAWed and the FSWed assemblies,

respectively, thus leading to fatigue crack initiation, particularly in low stress conditions.

VI. Acknowledgement

The authors acknowledge the Consortium de Recherche et d'Innovation en Transformation Métallique (CRITM 2016-2017 project #19), Mitacs Acceleration (project # IT06849), Bombardier Transportation, and Rio Tinto Aluminium for financial support in this research. The authors are particularly grateful to E. Marcoux, L.-D. Archambault, and S. Plamondon for their involvement in specimen preparation and testing. This work was part of a research program supported by the Aluminum Research Centre – REGAL, a strategic cluster creating synergies between Québec's aluminum researchers. The authors are particularly grateful to Dr. Christine BOHER (ICA) for tribology aspects in the contact region.

VII. Data availability

The raw and processed data required to reproduce these findings are available to download from Mendeley Data: doi:10.17632/tj6fs77n2g.1

VIII. References

1. Hatch, J. E. *Aluminum: Properties and Physical Metallurgy*. (ASM International, 1984). doi:10.1361/appm1984p001
2. Taub, A. I. & Luo, A. A. Advanced lightweight materials and manufacturing processes for automotive applications. *MRS Bull.* **40,** 1045–1053 (2015).
3. Çam, G. & Koçak, M. Progress in joining of advanced materials. *Int. Mater. Rev.* **43,** 1–44 (1998).
4. Kalpakjian, S., Schmid, S. R. & Sekar, K. S. V. *Manufacturing, Engineering and Technology*. (Pearson, 2014).
5. Barnes, T. A. & Pashby, I. R. Joining techniques for aluminium spaceframes used in automobiles: Part I - solid and liquid phase welding. *J. Mater. Process. Technol.* **99,** 62–71 (2000).
6. Mathers, G. *The welding of Aluminium and its alloys*. **1,** (Woodhead Publishing Limited, 2012).
7. Malin, V. Study of metallurgical phenomena in the HAZ of 6061-T6 aluminum welded joints. *Weld. J.* 305–318 (1995).
8. Myhr, O. R., Grong, Ø., Fjær, H. G. & Marioara, C. D. Modelling of the

microstructure and strength evolution in Al – Mg – Si alloys during multistage thermal processing. *Acta Mater.* **52,** 4997–5008 (2004).

9. Moreira, P. M. G. P., de Figueiredo, M. A. V. & de Castro, P. M. S. T. Fatigue behaviour of FSW and MIG weldments for two aluminium alloys. *Theor. Appl. Fract. Mech.* **48,** 169–177 (2007).
10. Ambriz, R. R., Barrera, G., García, R. & López, V. H. A comparative study of the mechanical properties of 6061-T6 GMA welds obtained by the indirect electric arc (IEA) and the modified indirect electric arc (MIEA). *Mater. Des.* **30,** 2446–2453 (2009).
11. Vargas, J. A., Torres, J. E., Pacheco, J. A. & Hernandez, R. J. Analysis of heat input effect on the mechanical properties of Al-6061-T6 alloy weld joints. *Mater. Des.* **52,** 556–564 (2013).
12. Stathers, P. A., Hellier, A. K., Harrison, R. P., Ripley, M. I. & Norrish, J. Hardness-tensile property relationships for HAZ in 6061-T651 aluminum. *Weld. J.* **93,** 301s–311s (2014).
13. Caruso, S. *et al.* Experimental comparison of the MIG, friction stir welding, cold metal transfer and hybrid laser-MIG processes for AA 6005-T6 aluminium alloy. *AIP Conf. Proc.* **1769,** (2016).
14. da Silva, J., Costa, J. M., Loureiro, A. & Ferreira, J. M. Fatigue behaviour of AA6082-T6 MIG welded butt joints improved by friction stir processing. *Mater. Des.* **51,** 315–322 (2013).
15. Mishra, R. S. & Ma, Z. Y. Friction stir welding and processing. *Mater. Sci. Eng. R Reports* **50,** 1–78 (2005).
16. Thomas, W. M. *et al.* Friction Stir Butt Welding. **Int. Paten,** U.S. Patent No. 5,460,317, Oct. 1995.
17. Liu, H. J., Fujii, H., Maeda, M. & Nogi, K. Tensile properties and fracture locations of friction-stir-welded joints of 6061-T6 aluminum alloy. *J. Mater. Sci. Lett.* **22,** 1061–1063 (2003).
18. Fujii, H., Cui, L., Maeda, M. & Nogi, K. Effect of tool shape on mechanical properties and microstructure of friction stir welded aluminum alloys. *Mater. Sci. Eng. A* **419,** 25–31 (2006).
19. Moreira, P. M. G. P. *et al.* Mechanical and metallurgical characterization of friction stir welding joints of AA6061-T6 with AA6082-T6. *Mater. Des.* **30,** 180–187 (2009).
20. Woo, W. & Choo, H. Softening behaviour of friction stir welded Al 6061-T6 and Mg AZ31B alloys. *Sci. Technol. Weld. Join.* **16,** 267–272 (2011).
21. Das, H., Chakraborty, D. & Kumar Pal, T. High-cycle fatigue behavior of friction stir butt welded 6061 aluminium alloy. *Trans. Nonferrous Met. Soc. China (English Ed.* **24,** 648–656 (2014).
22. Texier, D. *et al.* Near-surface mechanical heterogeneities in a dissimilar aluminum alloys friction stir welded joint. *Mater. Des.* **108,** 217–229 (2016).
23. Besel, Y. *et al.* Influence of local fatigue damage evolution on crack initiation behavior in a friction stir welded Al-Mg-Sc alloy. *Int. J. Fatigue* **99,** 151–162 (2017).
24. Shtrikman, M. M. Current state and development of friction stir welding Part 3. Industrial application of friction stir welding. *Weld. Int.* **22,** 806–815

(2008).

25. Shahri, M. M. & Sandström, R. Fatigue analysis of friction stir welded aluminium profile using critical distance. *Int. J. Fatigue* **32,** 302–309 (2010).
26. Masoumi, M., Zedan, Y., Texier, D., Jahazi, M. & Bocher, P. Effect of tool geometry and welding speed on mechanical properties of dissimilar AA2198 – AA2024 FSWed joint. *J. Manuf. Process.* **34,** 86–95 (2018).
27. Bridier, F., Stinville, J.-C., Vanderesse, N., Villechaise, P. & Bocher, P. Microscopic strain and crystal rotation measurement within metallurgical grains. *Key Eng. Mater.* **592–593,** 493–496 (2013).
28. Vanderesse, N., Lagacé, M., Bridier, F. & Bocher, P. An open source software for the measurement of deformation fields by means of digital image correlation. in (2013). doi:10.1017/S1431927613006090
29. Schindelin, J. *et al.* Fiji: an open-source platform for biological-image analysis. *Nat. Methods* **9,** 676–682 (2012).
30. Mohrbacher, H., Celis, J. P. & Roos, J. R. Laboratory testing of displacement and load induced fretting. *Tribol. Int.* **28,** 269–278 (1995).
31. Kuo, S. M. & Rigney, D. A. Sliding behavior of aluminum. *Mater. Sci. Eng. A* **157,** 131–143 (1992).
32. Baydoğan, M., Çimenoğlu, H. & Kayali, E. S. A study on sliding wear of a 7075 aluminum alloy. *Wear* **257,** 852–861 (2004).